Galindo, J.; Serrano, J.; García-Cuevas González, LM.; Medina-Tomás, N. (2021). Using a CFD analysis of the flow capacity in a twin-entry turbine to develop a simplified physics-based model. Aerospace Science and Technology. 112:1-9. https://doi.org/10.1016/j.ast.2021.106623

Using a CFD analysis of the flow capacity in a twin-entry turbine to develop a simplified physics-based model

José Galindo[a], José Ramón Serrano[a], Luis Miguel García-Cuevas[a], Nicolás Medina[a,*]

[a] *CMT – Motores Térmicos. Universitat Politècnica de València.*

Abstract

The current paper presents a flow behaviour analysis of twin-entry radial turbines by means of experimental measurements and computational fluid dynamics (CFD) simulations. The experimental data were measured at partial, unequal and full admission conditions, and was used to globally validate CFD simulations. The experimental results hinted towards considering twin-entry turbines as two separated single-entry turbines working in parallel when used in simplified physics-based models such as in one-dimensional simulations. After analysing the CFD results, a simple flow capacity model was developed, exploiting some of the observed characteristic phenomena to reduce the number of fitting parameters to their minimum while keeping its accuracy and extrapolation capabilities.

Keywords: Turbocharger, Twin-entry turbine, CFD analysis, Physics-based model, Flow capacity model

*Corresponding author.
E-mail address: nimeto@mot.upv.es

1. Introduction

Radial turbines are used in different applications such as wave energy converters [1], in organic Rankine cycles (ORC) [2], [3], in a distributed generation as microturbines [4], [5] or in generator sets [6]. But the most widely investigated use is in turbocharging reciprocating internal combustion engines (ICE), including range extenders for electric vehicles [7] or aircraft powerplants [8].

The emission of greenhouse gases such as CO_2, the particulate matter (PM) [9] and the emission of pollutant gases such as NO_x or unburnt hydrocarbons (HC) in ICE is continuously becoming more restricted. This can be clearly seen for passenger car vehicles with the new emissions standards, such as Euro 6 in the European Union [10], Bharat Stage 6 in India [11], China 5 and 6 in China [12] or Tier 3 in the United States of America [13]. Also, regulators and agencies worldwide are becoming more concerned about emissions from aeroengines and are preparing new inventories, regulations and standards, as can be seen in categories 1.A.3.a and 1.A.5.b of [14]. Meanwhile, the International Civil Aviation Organization (ICAO) is accepting new standards for regulating the emissions of CO_2 and non-volatile particulate matter.

One efficient technique to reduce these emissions is turbocharging [15]. As it increases the engine inlet pressure, the density of the intake air charge increases with favorable effects in the injection and combustion processes of fuel and in effective compression ratio of the assembly. In addition, for the same effective power, the engine size can be reduced and optimised maintaining its overall performance. This downsizing trend leads to less fuel consumption and, therefore, fewer emissions. The matching between turbocharger and ICE in design operational points has been well defined because of the reliability of fast 1D and 0D models, as detailed in Payri et al. [16] and Baines [17]. However, there are more difficulties to predict and to match the engine operation at turbocharger off-design conditions.

With the exponentially increasing computational power in the last decades, CFD simulations arise as an alternative solution to study turbochargers in steady-state conditions, as in Fürst et al. [18], but also in pulsating flow operation, as Palfreyman et al. [19], Ghenaiet et al. [20] and Galindo et al. [21, 22]. The pulsating flow simulations are becoming relevant because it is the real turbocharger operation conditions and they help to understand its performance. Other effects are even being simulated nowadays, such as compressor surge as in Huang et al. [23, 24], complex fluid-structure interactions that may lead to premature blade failure due to fatigue as in Zhao et al. [25], the noise emissions in complex compressor geometries as in Sharma et al. [26, 27] or the effect of an inlet bent torsional pipe on complex compressors as in Zhang et al. [28]. However, the 3D CFD simulations need to be validated with experimental data due to the simulations are not reliable on their own. They might calculate invalid results if they are not properly carried out. Once the simulations are validated with experimental data, their results will be considered valid.

Many researchers have also focused on turbocharger off-design conditions, where there are interesting different phenomena. Because of this fact, extrapolate these conditions from design operational points is difficult, but it can be modelled as in Serrano et al. [29], Binder et al. [30], Zhang et al. [31] and Walkingshaw et al. [32].

Traditionally, the most common configuration at the engine exhaust has been a single volute centripetal turbine. Nevertheless, this configuration presents some issues in multiple cylinder engines, as explained in Garret et al. [33]. As the flow is pulsating, there is interference between cylinders of adjacent firing order impeding the turbine to exploit all the available energy from the engine. Moreover, it imposes limits to the opening and closing angles of the exhaust valves and it reduces the volumetric efficiency.

These issues can be solved with twin-entry turbines, which are becoming the standard configuration in multiple cylinders, spark-ignition engines.

This kind of turbines have two volutes and the cylinders of adjacent firing order are connected to a different volute. It allows isolating the pulses and reducing their interference, but also some phenomena emerge in the space after the union of both volutes that must be analysed. Some authors have characterised these phenomena with different approaches, as Brinkert et al. [34], Yokoyama et al. [35], Romagnoli et al. [36], Cerdoun et al. [37, 38], Hajilouy-Benisi et al. [39], Aghaali et al. [40] and Chiong et al. [41]. Also, some authors have shown very interesting results regarding the effect of high-amplitude pulses inside the turbine in its efficiency, such as Xue et al. [42]: these effects may be included in simplified models for simplified one-dimensional simulations.

The current paper presents an experimental and CFD analysis of twin-entry turbines in order to better understand the phenomena occurring into their rotor and to extend to twin turbines the one-dimensional model proposed in [29] and to improve the model proposed in [43] by reducing significantly the number of fitting coefficients and increasing the physical meaning and generality of the proposed ones. In the CFD simulations, the mass flow passing through each volute has been followed within the geometry in order to corroborate the hypothesis based on experimental observation presented in Serrano et al. [44], which considers twin-entry turbines as two different single-entry, variable geometry turbines (VGT) working in parallel. This hypothesis will be considered valid if the degree of mixing of the mass flow from each volute within the rotor is small. Then, this one-dimensional model may be improved thanks to the flow behaviour observed in both experimental and CFD results. The model can be also coupled with other submodels of the turbocharger, taking into account the compressor quasi-steady map extrapolation [45], the heat transfer [46, 47, 48], the mechanical losses in the bearings [49] or the one-dimensional wave and mass accumulation effects [50].

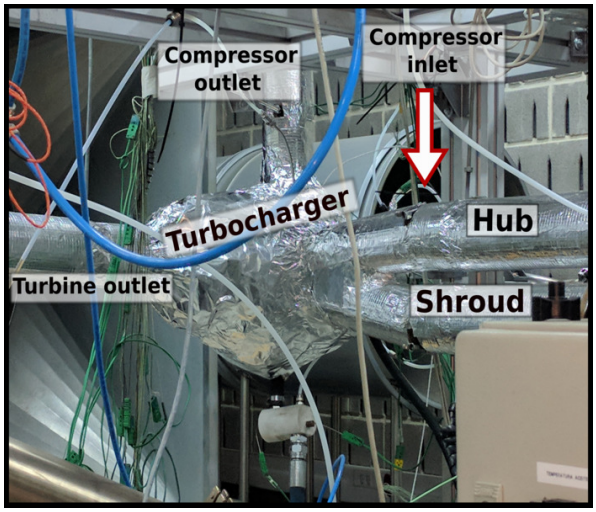

Figure 1: Gas Stand insulation.

2. Experimental Method

The first step to study twin volute turbines is to obtain reliable experimental data. Then, these data can be used for validating the results obtained in 3D CFD simulations. So, the turbine is measured in a gas stand.

The gas stand used for measuring the experimental data is specially designed for twin and double volute turbines. It utilizes compressed air that is split into two separated sets of pipe-work connected with each turbine volute, as explained in Serrano et al. [44]. In order to control and adjust with precision the mass flow rate of each set of pipework, there are two independent highly linear control valves. It allows assessing the impact of each entry on the overall performance in steady state conditions.

The compressed air is supplied by a two-stage, oil-free, centrifugal compressor. This compressor is powered by a 450 kW electric motor. The gas stand also has independent lubricating and coolant systems with adjustable mass flow. The turbocharger and all pipes are insulated in order to ensure an almost adiabatic operation, as shown in Fig. 1.

The main parameters such as pressure, temperature, turbocharger speed

Table 1: Gas stand measurement equipment and precision.

Variable	Sensor Type	Range	Expanded uncertainty
Gas Mass Flow	V-cone, Thermal and vortex	45-1230 $\mathrm{kg\,h^{-1}}$	¡ 2 %
Gas Pressure	Piezoresistive	0-500 kPa	12.5 hPa
Gas/Metal Temperature	K-type thermocouple	273-1500 K	1.5 K
Oil/coolant Pressure	Piezoresistive	0-500 kPa	12.5 hPa
Oil/coolant Temperature	RTD	173-723 K	¡ 0.5 K
Oil/coolant Mass Flow	Coriolis and Magnetic	Few tens $\mathrm{g\,s^{-1}}$	2 %
Turbocharger Speed	Inductive Sensor	¡ 300 krpm	500 rpm

and mass flow are measured with sensors located at essential sections, such as turbine inlets and turbine outlet. These sensors are listed in Table 1. The expanded uncertainty shown in the table uses a coverage factor of 3: assuming normal probability density distributions for the output of the sensors, the actual value of the measurements is expected to lie in an interval centred in the measured values with an amplitude equal to two times the expanded uncertainty with a confidence level of 99.7 %.

The admission conditions can be differentiated in 3 categories. Full ad-

mission conditions, when the mass flow rate is equal in both entries. Partial admission conditions, when there is mass flow passing only through one entry. Unequal admission conditions, when there is mass flow passing through both entries, but it has not got the same rate. In real operation, unequal admission conditions are the most common conditions

In order to describe these different mass flow admission conditions, a parameter that relates the mass flow passing through each volute should be defined. For a better understanding, the volute nearer the turbine hub will be named Hub Branch and the other volute Shroud Branch, as it is nearer the turbine shroud. So, the Mass Flow Ratio parameter (MFR) is defined in Eq. 1 as the ratio between the mass flow passing through the Shroud Branch and the total mass flow. Other authors prefer using the Reduced Mass Flow Ratio parameter (MFR_{red}) [51], which is the same ratio shown in Eq. 1 but using the reduced mass flow instead of the mass flow. Working with the MFR eases the experimental data acquisition while representing the same flow behaviour tendencies since the mass flow can be directly measured.

$$MFR = \frac{\dot{m}_{\mathrm{s}}}{\dot{m}_{\mathrm{s}} + \dot{m}_{\mathrm{h}}} \tag{1}$$

The MFR parameter will be 0 when there is only mass flow passing through the Hub Branch, 1 when there is only mass flow passing through the Shroud Branch, 0.5 when there are full admission conditions and the other values between 0 and 1 when there are unequal admission conditions. Then, the twin turbine experimental map can be represented with different values of MFR, as it is done in variable geometry turbines (VGT) with different nozzle vanes position, as explained in Serrano et al. [44]. The map represented in Fig. 2 shows the reduced mass flow versus the turbine expansion ratio for each branch with different MFR and reduced turbocharger speed. The expanded uncertainty of the reduced mass flow is less than 2%.

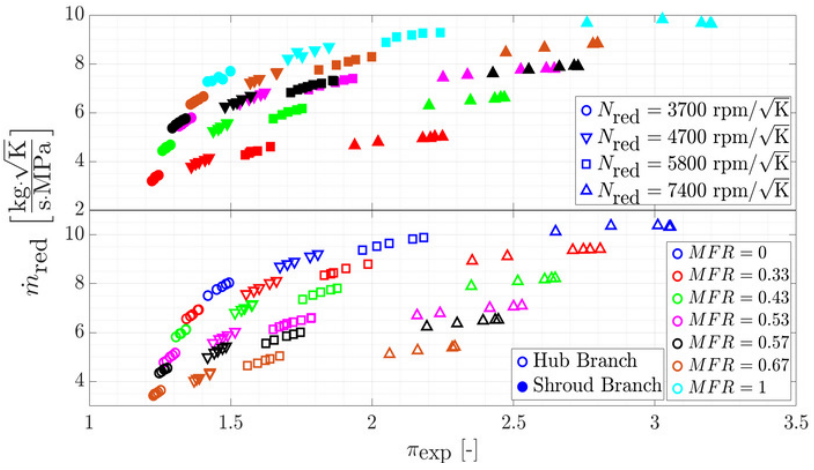

Figure 2: Experimental Map.

3. 1D Model

One-dimensional models are an interesting tool in order to simulate whole engines. They are able to catch most of the effects that are affecting the performance of the flow. Moreover, they have low computational cost, which allows using them in engine design and optimisation phases. The turbine behaviour in one-dimensional models is imposed using actuator disks for introducing the enthalpy and momentum source terms. The strength of these source terms are a function of the turbine operating point and the behaviour of the maps is represented in terms of flow capacity and efficiency. The manufacturer's maps provide the information needed by the models so they may be used directly as interpolation lookup tables. However, they are usually too narrow and only provide a few design points. Hence, an extrapolation model is needed in order to represent the whole turbine maps. Moreover, as the flow passing through one volute affects the performance of the flow passing through the other, the extrapolation model in the case of twin turbines will be even more complicated.

The turbine main stages are defined in Fig. 3. The volute inlet is defined as stage 0, the volute outlet/stator inlet is defined as stage 1, the stator

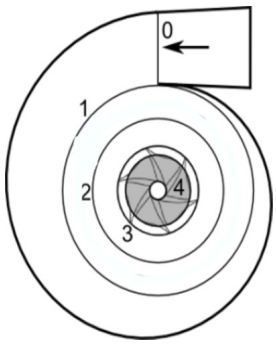

Figure 3: Twin volute turbine stages.

outlet is defined as stage 2, the rotor inlet is defined as stage 3 and the rotor outlet is defined as stage 4. As shown in Fig. 3, there is a vaneless stator.

The current paper is focused on the performance map represented in terms of flow capacity. In the one-dimensional model used [29], the turbine flow capacity performance is calculated as an equivalent nozzle which is characterized by an effective area, as shown in Eq. 2, where the numerical subscripts are referred to the corresponding stage and the subscript *Neq* is referred to the equivalent nozzle.

$$A_{Neq} = A_4 \sqrt{\frac{1 + \left(\frac{u_4}{v_{Neq}}\right)^2 - \left(\frac{u_3}{v_{Neq}}\right)^2 + \left(\frac{w_3}{v_{Neq}}\right)^2}{\left(\frac{A_4}{A_3}\right)^2 \left(\frac{\rho_4}{\rho_3}\right)^2 + 1}} \tag{2}$$

Some of these variables are hard to measure properly even in the design operational points. So, this effective area can be modelled using some simplifications detailed in Serrano et al. [29], obtaining the Eq. 3 that depends on geometrical parameters, the blade speed ratio (σ), some pressures and 4 calibration coefficients.

$$A_{Neq} = \frac{a \cdot A_4^{\text{geom}} \sqrt{1 + \dfrac{\sigma^2 \cdot \left[\left(\dfrac{D_4}{D_3}\right)^2 - 1\right] + b}{\eta_{\text{t,s}}}}}{\sqrt{1 + \left[c \cdot \dfrac{A_4^{\text{geom}}}{A_3^{\text{geom}} \cdot cos(\alpha_3)}\right]^2 \cdot \dfrac{\pi_{2,4}^{-2}}{\left[1 - \eta_{\text{t,s}} \cdot \left(1 - \pi_{2,4}^{\frac{1-\gamma}{\gamma}}\right)\right]^2}}} \tag{3}$$

where a is the rotor discharge coefficient, b is the ratio of rotor inlet relative kinetic energy and the nozzle isentropic kinetic energy, c is the ratio of rotor outlet and rotor inlet discharge coefficients and d is included through the term $\pi_{2,4} = 1 + d\,[\pi_{0t,4} - 1]$, being $d = (p_2 - p_4)/(p_{0t} - p_4)$. The value of these four coefficients can be set with the measured operational points information. Then, the effective area model will be adjusted.

These coefficients also depend on the working conditions of the turbine. So, CFD simulations along with the experimental results may be used to infer this dependency. Moreover, a simple model taking into account the effect of the *MFR* on the overall performance could be proposed.

4. CFD simulations

3D CFD simulations can be reliable when the geometry simulated is exactly the same than the measured. So, the twin turbine measured in the gas stand described in chapter 2 has been digitised as a CAD (Computer-Aided Design) model.

There are parts, as the rotor and the inlet and outlet ducts, easy to scan with a conventional 3D scanner. However, the volutes and the plenum at the rotor outlet are not as accessible as the other parts, so an inverse non-destructive process is proposed for digitising them. These parts are filled

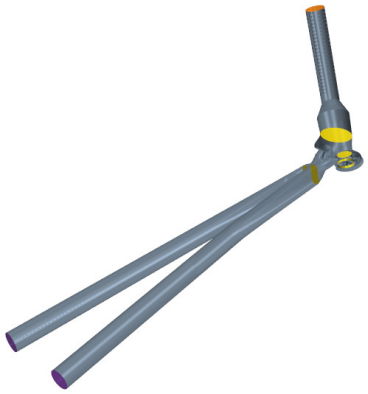

Figure 4: Twin Turbine Geometry.

with liquid silicone. When the silicone is cured, it is extracted. Then, these silicone moulds are the negative part of the volutes and the plenum at the rotor outlet and they can be scanned easily.

This process is not perfect and there may be some imperfections due to fissures or air bubbles in the moulds. Thus, these CAD parts should be carefully pre-processed before using them. Once all parts are properly prepared, they can be united in a unique CAD model, as shown in Fig. 4.

The mesh of this geometry should be fine enough in order to capture the correct results independently of the cell size. The regions near the wall should be meshed more accurately as well as the regions where more complicated phenomena are supposed, as the rotor tips. The mesh independence study carried out is shown in Table 2, controlling the pressure and temperature at the rotor inlet section in a case with *MFR* 0.53 and reduced turbocharger speed of $3700\,\mathrm{rpm\,K^{-0.5}}$.

The simulation results are almost independent of the mesh size for more than 5.5 million cells. So, the case with 5.5 million cells will be fine enough and it is shown in Fig. 5.

The simulations carried out are 3D unsteady Reynolds-Averaged Navier-Stokes (URANS) using the $k-\omega$ SST turbulence model. The equations are

Table 2: Mesh independence study. Pressure and temperature values at the rotor inlet section.

Number of cells ($\cdot 10^6$)	Total pressure [kPa]	Total temperature [K]
0.97	135.4	356.87
1.59	135.9	357.31
2.53	136.1	357.68
4.46	136.4	358.00
5.54	136.5	358.07
8.28	136.5	358.08

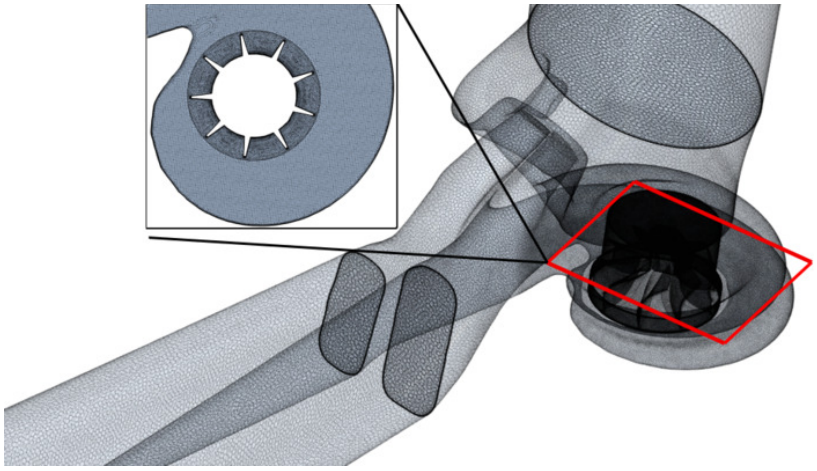

Figure 5: CAD model with final mesh.

solved with a second order, upwind, coupled flow solver, using the Roe's flux-difference splitting scheme adapted for use with Weiss-Smith preconditioning for all-speed flows. The air passing through each volute is differentiated using the multi-component gas option and both gases are modelled as non-reactive, ideal gases. This option allows following both gases separately within the geometry.

The boundary conditions are steady. The inlets boundary conditions are stagnation inlet, fixing the total pressure and temperature, the composition and the turbulence description. The outlet boundary condition is pressure outlet, giving the static pressure and temperature, the composition and the turbulence description for backflow. The values of the boundary conditions are extracted from the experimental data in order to compare properly both results. Four different turbocharger speed and 7 different *MFR* are selected, carrying out 28 simulations.

The simulations are started with a steady solver (RANS), using moving reference frames for simulating the motion of the rotor. Once these simulations are converged, they are used as initial conditions for the implicit unsteady solver (URANS), using rigid body motion to consider the motion of the wheel. The implicit unsteady solver is second order and has a constant time-step, which is defined in each case as the time spent in rotating one degree, following the steps detailed in Galindo et al. [52]. For each time-step, the simulations take 20 inner iterations in order to ensure the convergence of the residuals in the different equations.

4.1. CFD simulations validation

Once the simulations are converged, they need to be validated against experimental data since they are not reliable on their own. In order to represent the validity of the simulation results, Fig. 6 shows the reduced mass flow obtained in the simulations against the one from the experimental data. Dotted lines represent $\pm 2\,\%$ discrepancy, the measurements expanded uncertainty. The solid line represents perfect concordance.

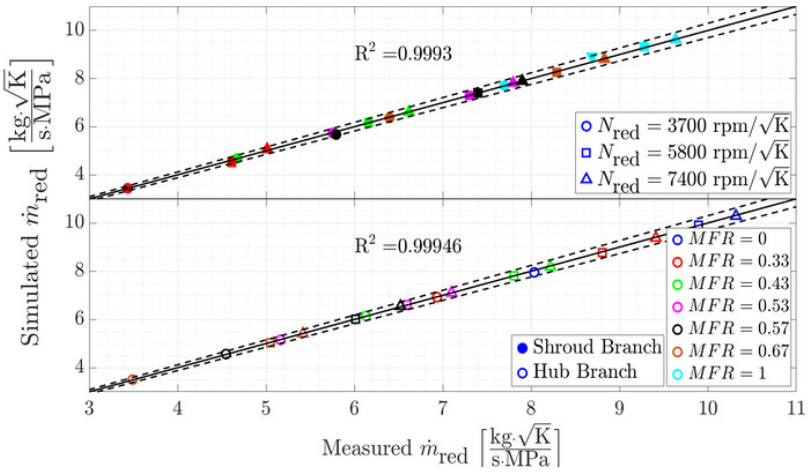

Figure 6: CFD and experimental map comparison.

There is good concordance between simulations and experimental data in all cases, even with extreme values of *MFR*. The error is lower than 3 % in the worst cases and the R^2 value is high in both branches. This error is a bit higher than the measurements expanded uncertainty, but only in a few cases.

In order to also validate the simulated energy results, the outlet total temperature can be compared between simulations and measurements, as shown in Fig. 7. Dotted lines represent a discrepancy of ±1.5 K. Despite there can be radial temperature non-uniformity, as explained in [53], 4 different thermocouples were used located at different insertion depths, producing an average that is expected to be representative of the actual mean at the measurement section. All simulated cases have less than 1.5 K of discrepancy, lower than the expanded uncertainty of the measurements.

Fig. 6 and Fig. 7 show that the error of the simulations is similar to or lower than the measurements expanded uncertainty. Thus, the simulations carried out could be considered reliable.

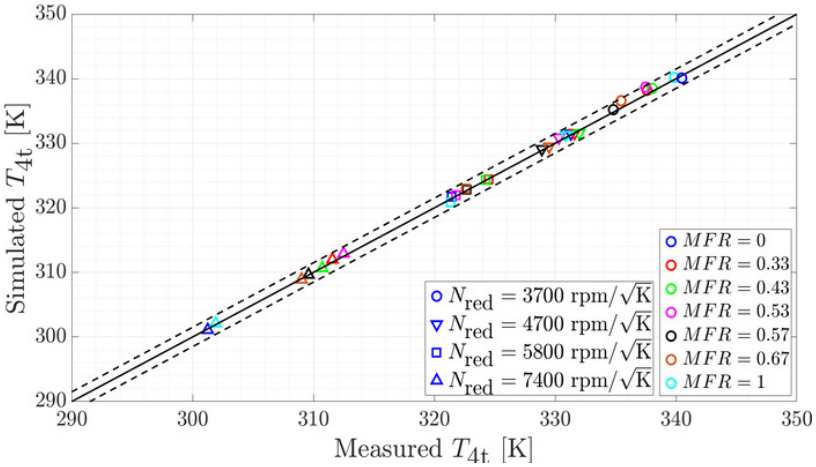

Figure 7: CFD and experimental outlet temperature comparison.

5. Analysis of the results

The behaviour of the flow passing through each volute within the rotor and all the turbine can be analysed qualitatively with the CFD simulations. The mass flow passing through each branch can be followed within the geometry by plotting the mass fraction of the flow that enters by one of the branches. As an example, Fig. 8 shows the mass fraction of air passing through the shroud branch in a section from the volutes until the rotor outlet for a case of *MFR* 0.57 and rotational speed 3700 rpm $K^{-0.5}$. The flow passing through each volute does not mix within the rotor significantly. The air from the shroud branch is basically maintained near the rotor shroud while the air from the hub branch is basically maintained near the rotor hub. The main mix is produced downstream of the rotor and it occurs in all the simulated cases. This behaviour is consistent with the hypothesis used in the reduced-order engine model [43], which models twin-entry turbines as two separated single volute VGT turbines working in parallel. This hypothesis was funded by the analysis of the experimental data, processed using the procedure described in [44]

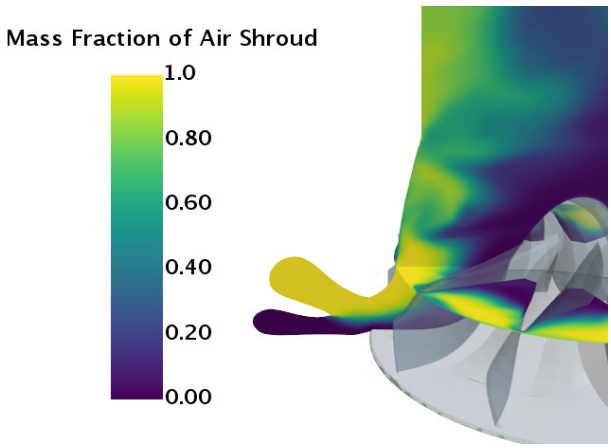

Figure 8: Local mass fraction of the gas from shroud branch.

5.1. Effect on the rotor inlet and outlet areas

Despite qualitatively all the cases show the same flow behaviour, the *MFR* variations change the volume percentage of each flow inside the rotor and it makes some differences between cases. This change can be represented by means of the area occupied by each branch flow at rotor inlet and outlet sections. Fig. 9 shows these area variations against the *MFR*.

The rotational speed effect on the area variation is very low in both inlet and outlet sections. However, the *MFR* effect on the area variation is very important. Moreover, this effect seems to have nearly linear trends, having a high R^2 value. So, an assumption of area linearity with the *MFR* can be made in the one-dimensional model for both inlet and outlet areas.

When observing the rotor outlet flow, the product of the average axial flow speed times the average density of the flow corresponding to one branch divided by the same product corresponding to the other branch was relatively close to 1, as observed in Fig. 10. It is close enough to 1 for considering that the trends of the effective outlet areas are almost linear with the *MFR* in the effective area model. When observing the rotor inlet flow, taking into account the average radial flow speed instead of the average axial flow speed,

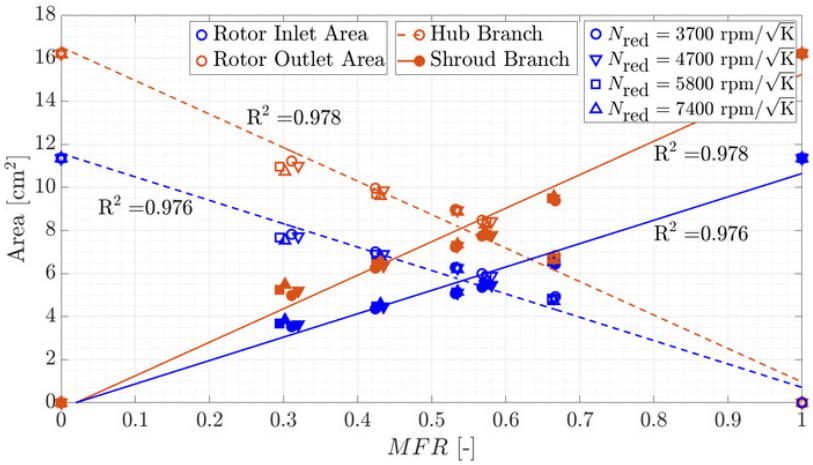

Figure 9: *MFR* and rotational speed influence on rotor inlet and outlet area occupied by each branch flow.

as shown also in Fig. 10, the behaviour of this ratio is similar. This flow behaviour at rotor inlet and outlet sections corroborate the assumption of area linearity with the *MFR*.

5.2. Rotor inlet and outlet areas effect on the flow capacity map

This flow behaviour may be important to introduce in the one-dimensional twin-entry turbine model. In order to take it into account, some geometrical parameters introduced into the code should be changed. The area at rotor inlet and outlet sections, shown in Fig. 11, follow the Eq. 4 and Eq. 5 respectively, being r_4^2 the wheel radius at rotor outlet, r_{nut}^2 the nut radius at rotor outlet, r_3 the wheel radius at rotor inlet and h_{blade} the blade height at rotor inlet.

$$A_3 = 2 \cdot \pi \cdot r_3 \cdot h_{\text{blade}} \tag{4}$$

$$A_4 = \pi \cdot (r_4^2 - r_{\text{nut}}^2) \tag{5}$$

The rotor inlet wheel radius is constant, so the blade height should be changed linearly in Eq. 4 in order to catch the flow behaviour against the

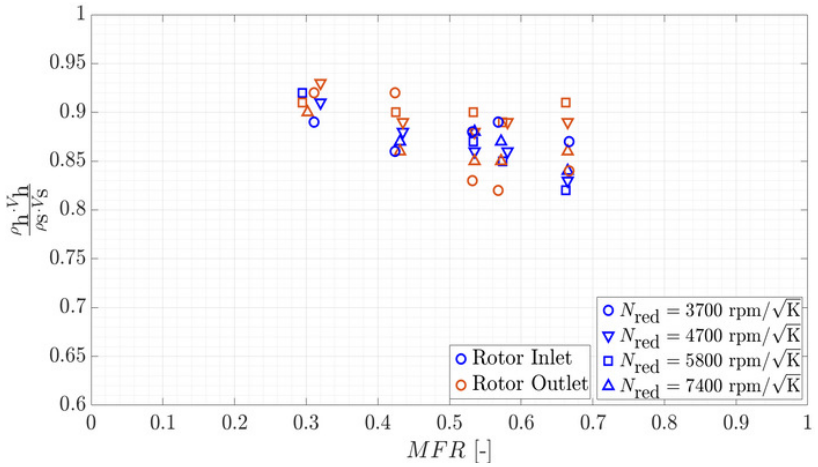

Figure 10: Rotor inlet and outlet area linearity with the *MFR* assumption corroboration.

MFR. In the shroud branch case, it will be linear with the *MFR*. In the hub branch case, it will be linear with parameter 1 – *MFR*.

In order to catch the flow behaviour against the *MFR* in the rotor outlet area, an intermediate radius (r_i) is defined as the frontier between both flows. In the shroud branch case, the intermediate radius will act as the nut radius at rotor outlet. In the hub branch case, the intermediate radius will act as the rotor outlet wheel radius.

$$A_{4_\mathrm{s}} = \pi \cdot (r_4^2 - r_i^2) \tag{6}$$

$$A_{4_\mathrm{h}} = \pi \cdot (r_i^2 - r_{\mathrm{nut}}^2) \tag{7}$$

This intermediate radius will be defined in order to reach a linear behaviour in the rotor outlet area and it will follow the Eq.8.

$$r_i = \sqrt{(1 - MFR) \cdot r_4^2 + MFR \cdot r_{\mathrm{nut}}^2} \tag{8}$$

These geometrical parameters changes are introduced into the effective area equation (Eq. 3) for both branches. Then, the calibration coefficients

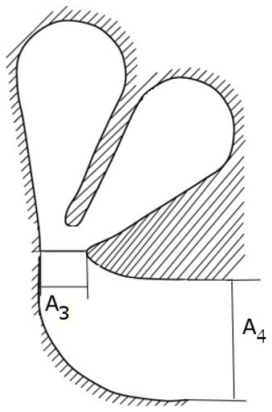

Figure 11: Area at rotor inlet and outlet sections.

are adjusted for each *MFR*, showing their dependence on the *MFR* in Fig. 12.

The a, b and c calibration coefficients have a nearly constant trend against the *MFR* for both branches. a is the rotor outlet discharge coefficient and the variation produced by the *MFR* has been introduced in the rotor outlet geometrical area with Eqs. 6 and 7. So, this calibration coefficient does not depend on the *MFR*. b is the relative kinetic energy ratio that depends on the rotor inlet geometrical area. As the effect of the *MFR* is already introduced in this area with Eq. 4, b does not depend on the *MFR*.

c is the ratio between rotor outlet and rotor inlet discharge coefficients. The rotor outlet discharge coefficient is nearly constant with the *MFR*, but the rotor inlet discharge coefficient depends on the *MFR*. However, the effect of the rotor inlet angle can be separated from the rotor inlet discharge coefficient and it depends directly on the *MFR*, as explained in [54]. If this effect is separated, the rotor inlet discharge coefficient has nearly constant trends against the *MFR*, but the direct dependence of the rotor inlet angle has to be included in the effective area equation dividing by the cosine of the rotor inlet angle, as shown in Eq 3. Then, the c calibration coefficient will have also a constant trend against the *MFR*.

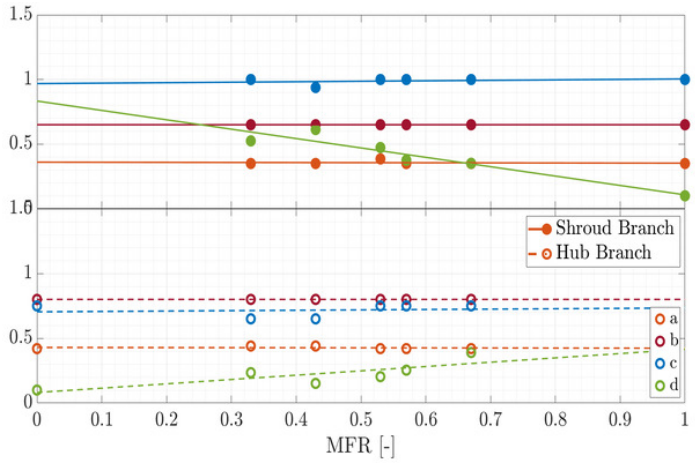

Figure 12: Calibration coefficients adjusted for each *MFR*.

The d calibration coefficient, however, has not constant trends against the *MFR*. It seems to have a nearly linear dependence, reducing its value while the mass flow in the studied branch increases. As d represents the ratio between the rotor static pressure drop and the whole turbine pressure drop, it actually shows the trend to increase pressure ratio in the vaneless space when the flow is increased in one branch vs the other. Fig. 12 shows how d value trends to 0 for the shroud branch when *MFR* increases since the mass flow of the shroud branch increases in comparison with the mass flow of the hub branch and there is a higher pressure ratio in the vaneless space. Due to the same reason, d value has the opposite trend for the hub branch, it trends to 0 when the *MFR* goes down.

Considering all these dependencies on the *MFR*, the twin-entry turbine one-dimensional model will only have 5 parameters per branch to adjust with the experimental data: one for each a, b and c calibration coefficients and two for d.

Then, using some information from the experimental data, the flow capacity map can be extrapolated toward different *MFR* values with this new approximation of the one-dimensional model. In Fig. 13 and Fig. 14, the ex-

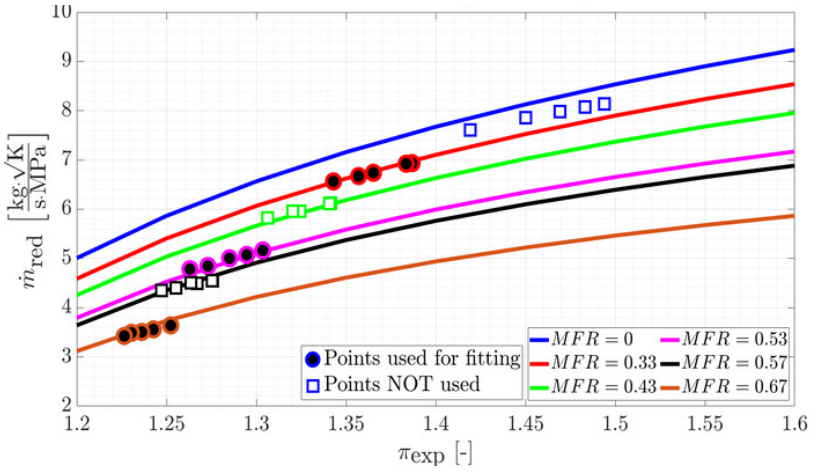

Figure 13: Hub Branch flow capacity extrapolation map.

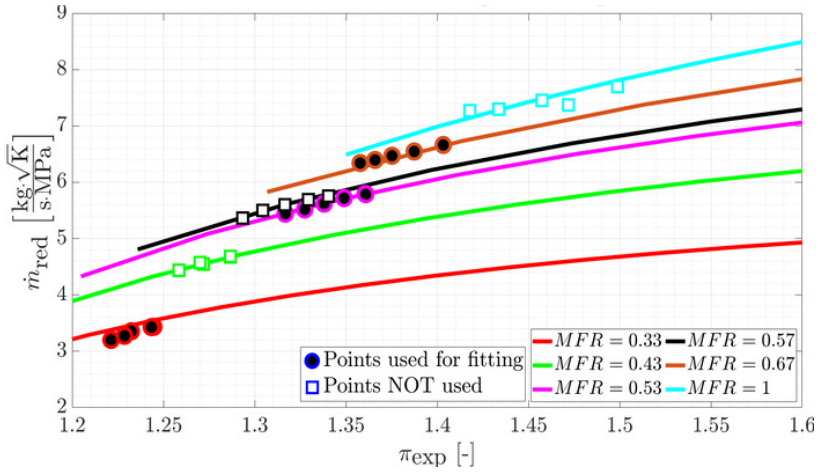

Figure 14: Shroud Branch flow capacity extrapolation map.

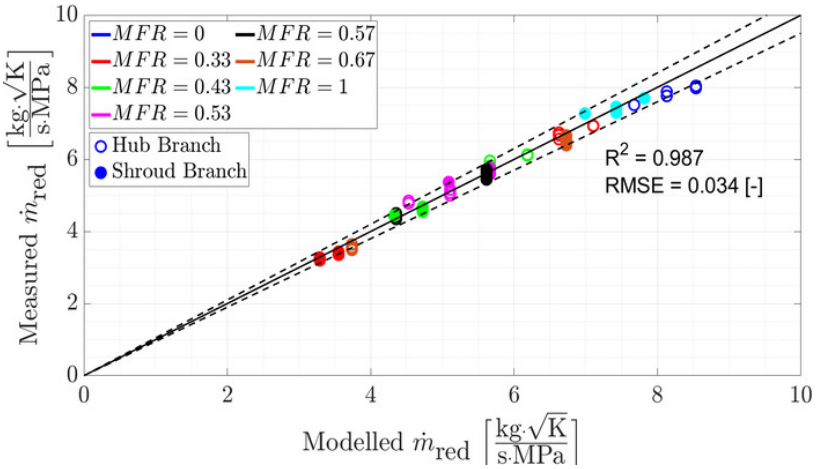

Figure 15: Measured vs Modelled reduced mass flow.

perimental data of *MFR* 0.33, 0.53 and 0.67 with reduced turbocharger speed of 3700 rpm $K^{-0.5}$ is used for fitting the calibration coefficients and the other *MFR* measured values with the same reduced speed are compared with the interpolation and extrapolation calculated with the one-dimensional model.

The interpolated *MFR* values (0.43 and 0.57) are almost coincident with the experimental data for both branches. The extrapolated *MFR* values (0 and 1) have small discrepancies with the experimental data, but they show good agreement. For a better estimation of the error committed, Fig. 15 compares directly the concordance between the measured and modelled reduced mass flow. The dotted lines represent ±5 % discrepancy.

There is good concordance between modelled points and experimental data. The R^2 value is high with relatively low root mean square error. The points used for fitting the calibration coefficients and those interpolated have very low error while the extrapolated points have an error lower than 5 % in almost all the cases. These extrapolated points worsen the overall root mean square error, but it is still small.

6. Conclusions

The current paper presents an improved methodology for generating twin-entry turbine flow capacity extrapolation maps based on experimental and CFD flow analysis. Both experimental and CFD results have been analysed and compared in order to improve the one-dimensional twin-entry turbine model.

The CFD simulations have been globally validated with the experimental data. The discrepancies in terms of reduced mass flow are lower than 3 %, which is an error similar to the experimental expanded uncertainty. The discrepancies in terms of rotor outlet temperature are lower than 1.5 K, which is an error lower than the experimental expanded uncertainty. Even in partial admission conditions, when there is a sudden expansion at the volute outlet, or at low expansion ratio, when there is some flow recirculation, the CFD results show good agreement in spite of coming from URANS simulations. These phenomena would be better captured with higher fidelity simulations as DES simulations.

The CFD simulations also have corroborated the hypothesis of study twin-entry turbines as two separated single volute VGT turbines in the one-dimensional model made from the experimental results. The simulations show that the flow passing through each branch does not fully mix with the other within the rotor.

The rotor inlet and outlet areas in the one-dimensional model have been modified in order to take into account the effect of the *MFR*. These areas have shown a nearly linear dependence on the *MFR* that is introduced changing some geometrical parameters for each branch as the blade height and the rotor outlet and rotor nut diameters. These changes make the one-dimensional twin-entry turbine model more physic since the effect of the *MFR* now is taken into account. Then, only five calibration parameters are needed per branch and they are adjusted with the experimental data.

The interpolation in the flow capacity maps has proven to be great while

the extrapolation is not perfect, but it shows good results with an error lower than 5 %. This extrapolation could be improved even more studying the efficiency maps since both the flow capacity and the efficiency maps are coupled. So, the next step is to study the twin-entry turbine efficiency maps.

Declaration of Competing Interest

None declared.

Acknowledgement

Nicolás Medina is partially supported through contract FPU17/02803 of Programa de Formación de Profesorado Universitario of Spanish Ministerio de Ciencia, Innovación y Universidades. This work has been partially supported by the "Ayuda a Primeros Proyectos de Investigación" (PAID-06-18), Vicerrectorado de Investigación, Innovación y Transferencia de la Universitat Politècnica de València (UPV), València, Spain. The authors wish to thank V. Ucedo for helping with the moulds, R. Carrascosa for his invaluable work during the experimental setup and campaign and P. Raga for his help with the setup of the CFD simulations. Finally, this work would not have been possible without the technical support of V. Lidó and J. Bustos of TODO-3D, who did a magnificent job scanning the turbine in 3D.

Nomenclature

Abbreviations

0D	Zero-dimensional
1D	One-dimensional
3D	Three-dimensional

CAD	Computational-aided design
CFD	Computational fluid dynamics
DES	Detached eddy simulations
HC	Hydrocarbons
ICAO	International Civil Aviation Organization
ICE	Internal combustion engine
ORC	Organic Rankine cycle
PM	Particulate matter
RANS	Reynols-averaged Navier-Stokes
URANS	Unsteady RANS
VGT	Variable geometry turbine

Roman letters

A	Area
a	Rotor discharge coefficient
b	Mass flow capacity fitting coefficient
c	Mass flow capacity fitting coefficient
D	Diameter
d	Mass flow capacity fitting coefficient
h	Height
$\dot{m}$	Mass flow rate
MFR	Mass flow ratio
N	Turbocharger speed

p	Pressure
r	Radius
T	Temperature
u	Blade tip speed
v	Absolute velocity
w	Relative velocity

Greek letters

α	Absolute velocity angle
γ	Specific heat capacities ratio
η	Efficiency
π	Expansion ratio
ρ	Density
σ	Blade to jet speed ratio

Subscripts and superscripts

0	Volute inlet station
1	Volute outlet station
2	Stator outlet station
3	Rotor inlet station
4	Rotor outlet station
blade	Blade
exp	Experimental

geom	Geometrical
h	Hub branch
i	Intermediate
N_{eq}	Equivalent nozzle
nut	Rotor outlet nut
red	Reduced
s	Shroud branch
t	Total
t,s	Total to static

References

References

[1] A. Falcao, L. Gato, J. Henriques, J. Borges, B. Pereiras, F. Castro, A novel twin-rotor radial-inflow air turbine for oscillating-watercolumn wave energy converters, Energy 93 (2015) 2116–2125. doi:10.1016/j.energy.2015.10.046.

[2] T. Yamamoto, T. Furuhata, N. Arai, K. Mori, Design and testing of the Organic Rankine Cycle, Energy 26 (2001) 239–251. doi:10.1016/S0360-5442(00)00063-3.

[3] S. H. Kang, Design and experimental study of ORC (Organic Rankine Cycle) and radial turbine using R245fa working fluid, Energy 41 (2012) 514–524. doi:10.1016/j.energy.2012.02.035.

[4] W. El-Khattam, M. Salama, Distributed generation technologies, definitions and benefits, Electric Power Systems Research 71 (2004) 119–128. doi:10.1016/j.epsr.2004.01.006.

[5] E. Facchinetti, D. Favrat, F. Marechal, Design and optimization of an innovative solid oxide fuel cell–gas turbine hybrid cycle for small scale distributed generation, Fuell Cells 14 (2014) 595–606. doi:10.1002/fuce.201300196.

[6] M. Malin, C. Redtenbacher, G. Lurf, N. Wermuth, A. Wimmer, Evaluation of strategies for highly transient operation of diesel-gas engines, in: Internal Combustion Engine Division Fall Technical Conference, ASME, 2018, Paper No: ICEF2018-9710, V001T01A010. doi:10.1115/ICEF2018-9710.

[7] A. Keromnes, B. Delaporte, G. Schmitz, L. L. Moyne, Development and validation of a 5 stroke engine for range extenders application, Energy Conversion and Management 82 (2014) 259–267. doi:10.1016/j.enconman.2014.03.025.

[8] A. P. Carlucci, A. Ficarella, D. Laforgia, A. Renna, Supercharging system behavior for high altitude operation of an aircraft 2-stroke diesel engine, Energy Conversion and Management 101 (2015) 470–480. doi:10.1016/j.enconman.2015.06.009.

[9] B. Giechaskiel, J. Vanhanen, M. Väkevä, G. Martini, Investigation of vehicle exhaust sub-23 nm particle emissions, Aerosol Science and Technology 51 (5) (2017) 626–641. doi:10.1080/02786826.2017.1286291.

[10] European Comission, Emissions in the automotive sector (2018).
URL https://ec.europa.eu/growth/sectors/automotive/environment-protection/emissions_en

[11] International Council On Clean Transportation, India Bharat Stage VI emission standards (2016).
URL https://theicct.org/sites/default/files/publications/India%20BS%20VI%20Policy%20Update%20vF.pdf

[12] H. Gong, Y. Ge, J. Wang, H. Yin, Light-duty vehicle emissions control: a brief introduction to the China 6 emissions standard, Johnson Matthey Technology Review 61 (2017) 269–278.

[13] Environmental Protection Agency, Environmental protection agency control of air pollution from motor vehicles: Tier 3 motor vehicle emission and fuel standards (2015).
URL https://www.epa.gov/regulations-emissions-vehicles-and-engines/final-rule-control-air-pollution-motor-vehicles-tier-3

[14] European Environment Agency, EEA Report No 13/2019, EMEP/EEA air pollutant emission inventory guidebook 2019 (2019). doi:10.2800/293657.

[15] N. Fraser, H. Blaxill, G. Lumsden, M. Bassett, Challenges for increased efficiency through gasoline engine downsizing, SAE International Journal of Engines 2 (2009) 991–1008. doi:10.4271/2009-01-1053.

[16] F. Payri, J. R. Serrano, P. Fajardo, M. A. Reyes-Belmonte, R. Gozalbo-Belles, A physically based methodology to extrapolate performance maps of radial turbines, Energy Conversion and Management 55 (2012) 149–163. doi:10.1016/j.enconman.2011.11.003.

[17] N. Baines, Turbocharger turbine pulse flow performance and modelling – 25 years on, in: 9th International conference on turbochargers and turbocharging, 2010, pp. 347–362.

[18] J. Fürst, Z. Žák, CFD analysis of a twin scroll radial turbine, in: EPJ Web of Conferences, Vol. 180, 2018. doi:10.1051/epjconf/201818002028.

[19] D. Palfreyman, R. Martinez-Botas, The pulsating flow field in a mixed flow turbocharger turbine: an experimental and computational study,

Journal of Turbomachinery 127 (1) (2005) 144. doi:10.1115/1.1812322.

[20] A. Ghenaiet, M. Cerdoune, Simulations of steady and unsteady flows through a twin-entry radial turbine, in: Turbo Expo: Power for Land, Sea and Air, Vol. Paper No: GT2014-25764, V02DT42A015, ASME, 2014. doi:10.1115/GT2014-25764.

[21] J. Galindo, P. Fajardo, R. Navarro, L. M. Garcia-Cuevas, Characterization of a radial turbocharger turbine in pulsating flow by means of CFD and its application to engine modelling, Applied Energy 103 (2013) 116–127. doi:10.1016/j.apenergy.2012.09.013.

[22] J. Galindo, A. Tiseira, P. Fajardo, L. M. Garcia-Cuevas, Development and validation of a radial variable geometry turbine model for transient pulsating flow applications, Energy Conversion and Management 85 (2014) 190–203. doi:10.1016/j.enconman.2014.05.072.

[23] Q. Huang, M. Zhang, X. Zheng, Compressor surge based on a 1D-3D coupled method. Part 1: Method establishment, Aerospace Science and Technology 90 (2019) 342–356. doi:10.1016/j.ast.2019.04.040.

[24] Q. Huang, M. Zhang, X. Zheng, Compressor surge based on a 1D-3D coupled method. Part 2: Surge investigation, Aerospace Science and Technology 90 (2019) 289–298. doi:10.1016/j.ast.2019.04.042.

[25] B. Zhao, X. Shi, H. Sun, M. Qi, P. Song, Effects of grooved vanes on shock wave and forced response in a turbocharger turbine, International Journal of Engine Research (2019). doi:10.1177/1468087419879265.

[26] S. Sharma, J. García-Tíscar, J. M. Allport, S. Barrans, A. K. Nickson, Effects of ported shroud casing treatment on the acoustic and flow behaviour of a centrifugal compressor, International Journal of Engine Research (2019). doi:10.1177/1468087419880431.

[27] S. Sharma, J. García-Tíscar, J. M. Allport, S. Barrans, A. K. Nickson, Evaluation of modelling parameters for computing flow-induced noise in a small high-speed centrifugal compressor, Aerospace Science and Technology (2020). doi:10.1016/j.ast.2020.105697.

[28] H. Zhang, C. Yang, C. Yang, H. Zhang, L. Wang, J. Chen, Inlet bent torsional pipe effect on the performance and stability of a centrifugal compressor with volute, Aerospace Science and Technology 93 (2019). doi:10.1016/j.ast.2019.105322.

[29] J. R. Serrano, F. J. Arnau, L. M. Garcia-Cuevas, A. Dombrovsky, H. Tartoussi, Development and validation of a radial turbine efficiency and mass flow model at design and off-design conditions, Energy Conversion and Management 128 (2016) 281–293. doi:10.1016/j.enconman.2016.09.032.

[30] N. Binder, X. Carbonneau, P. Chassaing, Off-design considerations through the properties of some pressure-ratio line of radial inflow turbines, International Journal of Rotating Machinery (2008) 1–8doi:10.1155/2008/273296.

[31] C. Zhang, X. Dong, X. Liu, Z. Sun, S. Wu, Q. Gao, C. Tan, A method to select loss correlations for centrifugal compressor performance prediction, Aerospace Science and Technology 93 (2019). doi:10.1016/j.ast.2019.105335.

[32] J. Walkingshaw, S. Spence, J. Ehrhard, D. Thornhill, An investigation into improving off-design performance in a turbocharger turbine utilizing non-radial blading, in: Turbo Expo: Power for Land, Sea and Air, ASME, 2011, pp. 2023–2032, Paper No: GT2011-45717. doi:10.1115/GT2011-45717.

[33] T. Garret, K. Newton, W. Steeds, Turbocharging and supercharging, Motor Vehicle (2000) 556–589.

[34] N. Brinkert, S. Sumser, S. Weber, K. Fieweger, A. Schulz, H. J. Bauer, Understanding the twin scroll turbine: flow similarity, Journal of Turbomachinery 135 (2013) 021039. doi:10.1115/1.4006607.

[35] T. Yokoyama, T. Hoshi, T. Yoshida, K. Wakashima, Development of twin-entry scroll radial turbine for automotive turbochargers using unsteady numerical simulation, 11th International Conference on Turbochargers and Turbocharging (2014) 471–478doi:10.1533/978081000342.471.

[36] A. Romagnoli, R. F. Martinez-Botas, S. Rajoo, Steady state performance evaluation of variable geometry twin-entry turbine, International Journal of Heat and Fluid Flow 32 (2) (2011) 477–489. doi:10.1016/j.ijheatfluidflow.2010.12.002.

[37] M. Cerdoun, A. Ghenaiet, Characterization of a twin-entry radial turbine under pulsatile flow condition, International Journal of Rotating Machinery (2016) 1–15doi:0.1155/2016/4618298.

[38] M. Cerdoun, A. Ghenaiet, Unsteady behaviour of a twin entry radial turbine under engine like inlet flow conditions, Applied Thermal Engineering 130 (2018) 93–111. doi:10.1016/j.applthermaleng.2017.11.001.

[39] A. Hajilouy-Benisi, M. Rad, M. R. Shahhosseini, Flow and performance characteristics of twin-entry radial turbine under full and extreme partial admission conditions, Archive of Applied Mechanics 79 (12) (2009) 1127–1143. doi:10.1007/s00419-008-0295-5.

[40] H. Aghaali, A. Hajilouy-Benisi, Experimental and theoretical investigation of twin-entry radial inflow gas turbine with unsymmetrical volute under full and partial admission conditions, in: Turbo Expo: Power for Land, Sea and Air, ASME, 2007, pp. 1099–1107, Paper No: GT2007-27807. doi:10.1115/GT2007-27807.

[41] M. S. Chiong, S. Rajoo, R. F. Martinez-Botas, A. W. Costall, Engine turbocharger performance prediction: One-dimensional modelling of a twin entry turbine, Energy Conversion and Management 57 (2012) 68–78. doi:10.1016/j.enconman.2011.12.001.

[42] Y. Xue, M. Yang, R. F. Martinez-Botas, B. Yang, K. Deng, Unsteady performance of a mixed-flow turbine with nozzled twin-entry volute confronted by pulsating incoming flow, Aerospace Science and Technology 95 (2019). doi:10.1016/j.ast.2019.105485.

[43] J. R. Serrano, F. J. Arnau, L. M. Garcia-Cuevas, V. Samala, A robust adiabatic model for a quasi-steady prediction of far-off non-measured performance in vaneless twin-entry or dual-volute radial turbines, Applied Sciences 10 (1955) (2020). doi:10.3390/app10061955.

[44] J. R. Serrano, F. J. Arnau, L. M. Garcia-Cuevas, V. Samala, L. Smith, Experimental approach for the characterization and performance analysis of twin entry radial-inflow turbines in a gas stand and with different flow admission conditions, Applied Thermal Engineering 159 (2019). doi:10.1016/j.applthermaleng.2019.113737.

[45] J. Galindo, R. Navarro, L. M. García-Cuevas, D. Tarí, H. Tartoussi, S. Guilain, A zonal approach for estimating pressure ratio at compressor extreme off-design conditions, International Journal of Engine Research 20 (4) (2019) 393–404. doi:10.1177/1468087418754899.

[46] F. Payri, P. Olmeda, F. J. Arnau, A. Dombrovsky, L. Smith, External heat losses in small turbochargers: Model and experiments, Energy 71 (2014) 534 – 546. doi:10.1016/j.energy.2014.04.096.

[47] J. R. Serrano, P. Olmeda, F. J. Arnau, A. Dombrovsky, L. Smith, Turbocharger heat transfer and mechanical losses influence in predicting engines performance by using one-dimensional simulation codes, Energy 86 (2015) 204 – 218. doi:10.1016/j.energy.2015.03.130.

[48] A. Gil, A. Tiseira, L. M. García-Cuevas, T. Rodríguez Usaquén, G. Mijotte, Fast three-dimensional heat transfer model for computing internal temperatures in the bearing housing of automotive turbochargers, International Journal of Engine Research (2018). doi:10.1177/1468087418804949.

[49] J. R. Serrano, P. Olmeda, A. Tiseira, L. M. García-Cuevas, A. Lefebvre, Theoretical and experimental study of mechanical losses in automotive turbochargers, Energy 55 (0) (2013) 888 – 898. doi:10.1016/j.energy.2013.04.042.

[50] J. R. Serrano, F. J. Arnau, L. M. García-Cuevas, P. Soler, Experimental validation of a one-dimensional twin-entry radial turbine model under non-linear pulse conditions, International Journal of Engine Research (2019). doi:10.1177/1468087419869157.

[51] N. Schorn, The radial turbine for small turbocharger applications: Evolution and analytical methods for twin-entry turbine turbochargers, SAE Int. J. Engines 7 (2014). doi:10.4271/2014-01-1647.

[52] J. Galindo, S. Hoyas, P. Fajardo, R. Navarro, Set-up analysis and optimization of CFD simulations for radial turbines, Engineering Applications of Computational Fluid Mechanics 7 (2013) 441–460. doi:10.1080/19942060.2013.11015484.

[53] S. Marelli, V. Usai, M. Capobianco, G. Montenegro, A. D. Torre, A. Onorati, Direct evaluation of turbine isentropic efficiency in turbochargers: CFD assisted design of an innovative measuring technique, SAE Technical Paper (2019). doi:10.4271/2019-01-0324.

[54] J. Galindo, J. R. Serrano, L. M. García-Cuevas, N. Medina, Experimental and computational analysis of the flow passing through each branch of a twin-entry turbine, 14th International Conference on Turbochargers and Turbocharging (2020).